Chapter 2

ION - SOLID INTERACTIONS

Lucille A. Giannuzzi[1], Brenda I. Prenitzer,[2] Brian W. Kempshall[2]
[1]FEI Company, Hillsboro, OR 97124, [2]Nanospective Inc., Orlando FL 32826.

Abstract: In this chapter we summarize reactions that take place when an energetic ion impinges on a target surface. The results based on equations that are usually used to estimate ion range and ion sputtering in amorphous materials are presented. A discussion on ion channeling and ion damage in crystalline materials is presented. The problems of redeposition associated with an increase in sputtering yield within a confined trench are presented. Knowledge of ion - solid interactions may be used to prepare excellent quality FIB milled surfaces.

Key words: secondary electron imaging, secondary ion imaging, ion range, incident angle, ion energy, sputtering, backsputtering, channeling, ion damage, amorphization, redeposition

1. INTRODUCTION

The ability to mill, image, and deposit material using a focused ion beam (FIB) instrument depends critically on the nature of the ion beam - solid interactions. Figure 1 shows a schematic diagram illustrating some of the possible ion beam/material interactions that can result from ion bombardment of a solid. Milling takes place as a result of physical sputtering of the target. An understanding of sputtering requires consideration of the interaction between an ion beam and the target. Sputtering occurs as the result of a series of elastic collisions where momentum is transferred from the incident ions to the target atoms within a collision cascade region. A surface atom may be ejected as a sputtered particle if it receives a component of kinetic energy that is sufficient to overcome the surface binding energy (SBE) of the target material. A portion of the ejected atoms may be ionized and collected to either form an image or be mass analyzed (see chapters on FIB/SIMS). Inelastic interactions also occur as the result of

ion bombardment. Inelastic scattering events can result in the production of phonons, plasmons (in metals), and the emission of secondary electrons (SE). Detection of the emitted SE is the standard mode for imaging in the FIB; however, as previously mentioned secondary ions (SI) can also be detected and used to form images.

In general, the number of secondary electrons generated per incident ion is ~ 1 and is 10-1000x greater than the number of secondary ions generated per incident ion (Orloff et al., 2003). A comparison of an ion beam induced SE image and an ion beam induced SI image from the same region of the eye of a typical Florida bug is shown in figure 2. Note the complementary information that may be obtained using both of these imaging conditions. Non-conducting regions of a sample will accumulate a net positive charge as a result of the impinging Ga^+ ions. The net positive charge will inhibit the escape of SEs emitted from the surface. This type of charging artifact is observed as dark contrast in the image. For example, the regions around the bug eye in the lower left shows charging artifacts in the SE image, but are clearly delineated in the SI image. In addition, the dark feature on top of the eye shown in the SE image also shows evidence of charging, while the SI image clearly shows the details of the feature. Thus, secondary ion imaging is a useful alternative to circumvent charging artifacts during FIB imaging and milling of non-conducting samples.

Interactions between the incident ion and the solid occur at the expense of the initial kinetic energy of the ion. Consequently, if the ion is not backscattered out of the target surface, the ion will eventually come to rest, implanted within the target at some depth (i.e., R_p as shown in Figure 1) below the specimen surface.

The quality of the milled cuts or CVD deposited regions depends critically on the interactions between the impinging ion beam and the target. Thus, understanding the basics of ion beam-solid interactions may greatly enhance the ability to achieve optimum results using an FIB system. In this chapter, we present a brief introduction to the interactions that occur when an energetic ion impinges on a solid target surface. The interactions summarized below are those that are important within the energy regime that is characteristically used in the FIB (~ 5-50 keV). More extensive details on ion-solid interactions are available elsewhere (see e.g., Orloff et al., 2003; Nastasi et al., 1996).

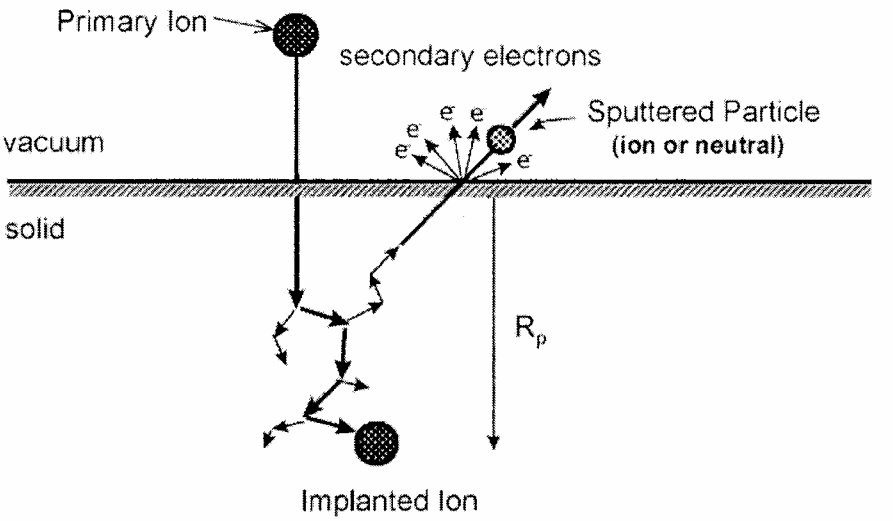

Figure 2-1. Schematic diagram of the sputtering process and ion-solid interactions (adapted from Nastasi et al., 1996).

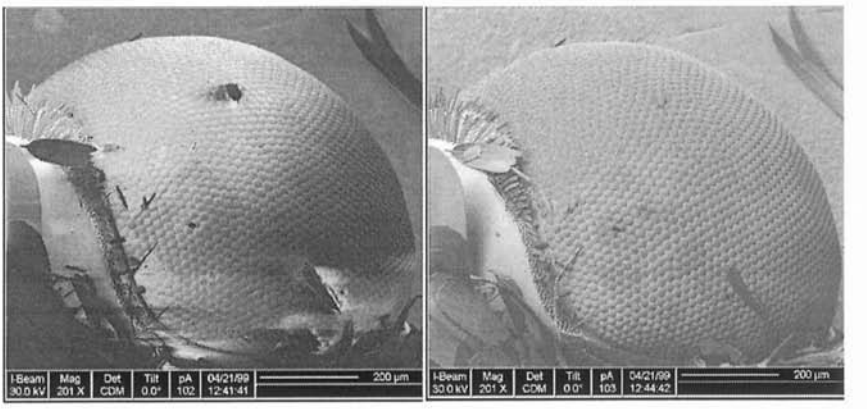

Figure 2-2. Ion induced (left) secondary electron and (right) secondary ion images of the eye of a typical Florida bug.

2. THE RANGE OF IONS IN AMORPHOUS SOLIDS

When a solid material is bombarded with an ion beam, a number of mechanisms operate to slow the ion and dissipate the energy. These mechanisms can be subdivided into two general categories: (i) nuclear energy losses, and (ii) electronic energy losses. Nuclear energy transfer occurs in discrete steps as the result of elastic collisions where energy is imparted from the incident ion to the target atom by momentum transfer. Electronic energy losses occur as the result of inelastic scattering events where the electrons of the ion interact with the electrons of the target atoms. The rate of ion energy loss per unit path length, dE/dx, and has both nuclear and electronic contributions. However, sputtering in typical FIB processes occur in energy ranges that are dominated by nuclear energy losses. Therefore, it is sufficient to present ion-solid interactions due only to the nuclear energy loss of ions as discussed below. The interested reader may find a discussion on electronic energy losses elsewhere (e.g., Nastasi et al. 1996).

2.1 The Concept of Ion Range

There tends to be some ambiguity in the terms and conventions used to describe ion range data. There are several distinctions between closely related concepts that should be emphasized. The first source of confusion can stem from the shear number of parameters used to quantify the distance that an energetic ion travels in a solid: i.e., range (R), projected range (R_p), penetration depth (X_s), transverse projected range (R_p^t), spreading range (R_s), radial range (R_r), and projected range straggling (ΔR_p). It is simplest to establish range definitions in terms of the interaction of a single ion with a solid. A sound physical interpretation of these definitions allows their application to actual ion beam processes that enlist the action of many ions. Ultimately, the implantation behavior of a single ion can be extrapolated to reflect the implantation behavior of multiple ions in terms of population dynamics.

Beginning with definitions as applied to a single ion, the range (R) described by Equation 1, is defined as the integrated distance that an ion travels while moving in a solid, and is inversely related to its stopping power (Nastasi et al., 1996; Ziegler et al., 1985; Townsend et al., 1976). The stopping cross-section, S(E), is defined as S(E) = (dE/dx)/N, where N is the atomic density. The stopping cross-section may be thought of as the energy loss rate per scattering center.

$$R = \int_{E_0}^{0} \frac{dE}{dE/dx} = \int_{E_0}^{0} \frac{dE}{NS(E)} \quad (1)$$

Thus, R may be defined by the path length for a single ion as illustrated in the schematic diagram in Figure 3. Examination of figure 3 reveals that R is not the same as the longitudinal projected range for a single ion (R_p). R_p for a single ion is the projection of its R onto its incident trajectory vector (sometimes denoted as I_o). Figure 3 is the generic case for arbitrary incidence angle. Only when $\theta = 0^\circ$ (i.e., when the beam is normal to the surface), does R_p equal the implant depth (X_s) as measured perpendicular to the target surface (Nastasi et al., 1996; Gibbons et al., 1975). It should be noted that the statistical R_p, as applied to a collection of ions, is the quantity most frequently used to describe depth for an ion implant. Where R_p for a distribution of ions in a target material is most commonly defined by convention, as the distance measured along the incident ion trajectory at which the highest concentration of implanted ions will be found. It should be noted that the statistical value, X_s, is a more pertinent value of interest for understanding sidewall implantation (e.g., in a FIB prepared TEM specimen).

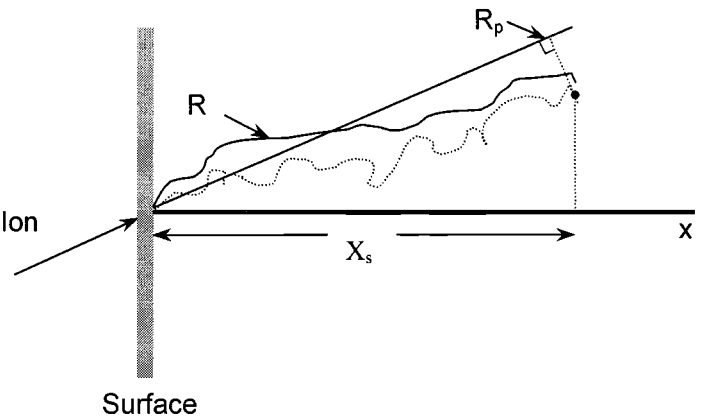

Figure 2-3. A 2D schematic diagram of the path of a single ion that has entered the target at an angle not equal to the surface normal. Note that $R_p = X_s$ only when the incident angle is 0°. (adapted from Mayer, et al. 1970)

A summary of the parameters of interest for the range of travel of an incident ion for the more general 3D case of a single energetic particle

entering the solid at (0,0,0) and coming to rest at (x_s, y_s, z_s) is shown in the schematic diagram in figure 4 may be described as follows (Nastasi et al., 1996):

- R is the *range* as defined above
- R_p is the *projected range* for a single ion as defined above
- X_s is the projected range as measured along a vector normal to the surface as shown in figure 3.
- R_r is the *radial range* which is the distance from (0,0,0) to (x_s, y_s, z_s). Note: R_p is the projection of R_r on the direction vector of I_o.
- R is the *spreading range* which is the distance between (0,0,0) and the projection of R_r on the surface (the yz plane)
- R_p^t is the *transverse projected range* which is the vector connecting R_r and R_p.

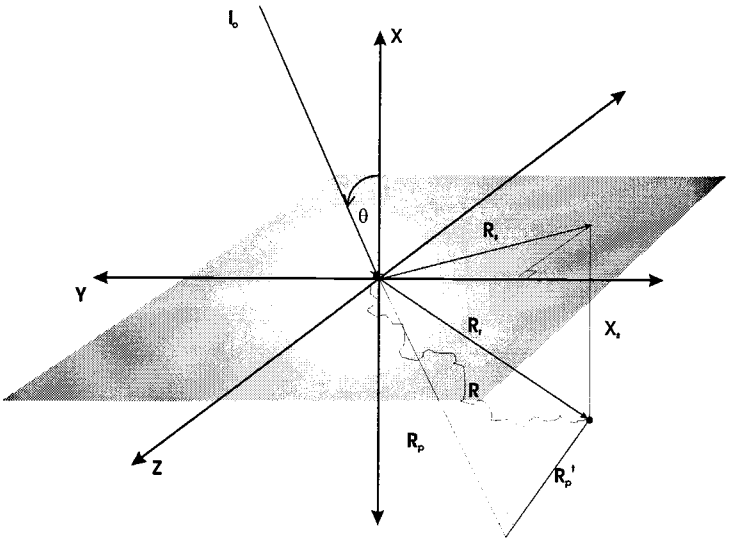

Figure 2-4. A 3D representation of a path taken by an ion that enters a solid at angle θ from the surface normal. (Adapted from Eckstein, 1991)

Although the range definitions above were presented in terms of the penetration behavior of a single ion, ion beam processes require the collective effect of a large number of ions. For the energy ranges associated with FIB applications, stopping of an energetic projectile is a random process, and the range distribution of a sufficiently large population of ions is statistical in nature. The probability function describing implant depth distributions is approximately Gaussian when dealing with relatively low implanted ion concentrations (i.e., less than a few atomic percent) and in the absence of crystallographic channeling effects (Nastasi et al., 1996). The mean of the distribution is the projected range, R_p, and the standard deviation is the projected range straggle, ΔR_p. In a normal Gaussian range distribution of implanted ions, the the largest number of ions will be located at R_p and ΔR_p is $R_p/2.35$ (Nastasi et al., 1996). It should be noted that the range distribution tends to deviate from a Gaussian profile in the presence of either crystallographic orientation effects or high ion doses. Ion channeling causes the depth distribution to be skewed because channeled ions penetrate to depths several times greater than R_p

2.2 Modeling Ion-Solid Interactions in Amorphous Materials

2.2.1 The Collision Cascade

When a target atom is knocked from its position, it can contribute to the collision cascade, (i.e., the moving sea of particles) within a solid under ion bombardment. Sputtering occurs if sufficient momentum is transferred from the collision cascade to a surface or near surface particle. The main parameters that govern the energy loss rate of the incident ion are its energy (E_o), the atomic masses (M_1 and M_2), and atomic numbers (Z_1 and Z_2), of the ion and the target atoms, respectively. The nature of the cascade is dependent on the ratio of the target to ion masses (M_2/M_1) and the incident ion energy. The classification of collision cascades is divided into three regimes. Regime I is called the single knock-on regime, and occurs when either $M_1 << M_2$ or E_o is low. In this regime, the recoil atoms do not receive enough energy to generate a cascade and sputtering is minimal. Regime II is the linear cascade regime where E_o is moderate and $M_1 \approx M_2$. In this regime recoil atoms receive enough energy to generate a cascade, but the density of moving atoms is dilute enough to disregard both multiple collisions and collisions between moving atoms. Linear assumptions that lead to the binary collision approximation are valid in regime II. The linear collision cascade model of regime II is where the FIB generally operates. Regime III is called

the spike regime where $M_1 >> M_2$ and/or E_o is large. The result is that the majority of the atoms within the spike volume move during the collision cascade. Regime III is seldom reached during conventional FIB operation (Townsend et al., 1976).

2.2.2 Modeling Energy Loss in Ion-Solid Interactions

The dominant mechanism of energy loss in the energy range used in the FIB process (e.g., 5-50 keV) involves elastic interactions between the ion and a screened nucleus (i.e., nuclear stopping). This is generally modeled using a two-body billiard ball collision model. The "collision" is the distance of closest approach governed by interatomic potentials between the incident ion and the target atom. The influence that the nuclear charge of one atom can exert on another atom is modulated by the shielding efficiency of the orbital electrons. Thus, physical phenomena tend to exhibit periodic fluctuations based on electronic structure and atomic radii of the atoms under consideration.

With each collision, the incident ion losses energy and changes direction by an angle, Θ. Using conservation of momentum in a center of mass coordinate system, the recoil energy of the struck atom is the energy transferred to target atom, T, as shown in equation (2).

$$T = \frac{4M_1M_2}{(M_1+M_2)^2} E_o Sin^2\frac{\Theta}{2} = \frac{4E_cM_c}{M_2} Sin^2\frac{\Theta}{2} \qquad (2)$$

In equation (2), $E_c = (E_oM_2)/(M_1+M_2)$, and $M_c = (M_1M_2)/(M_1+M_2)$. The final angle of scatter, Θ, may be expressed in terms of the initial center of mass energy, E_c, the potential, V(r), and an impact parameter, p, as shown by equation (3) (Ziegler et al. 1984), where r_{min} is the distance of closest approach during the collision.

$$\Theta = \int_{r_{min}}^{\infty} \frac{pdr}{r^2\sqrt{\left[1-\frac{V(r)}{E_c}-\frac{p^2}{r^2}\right]}} \qquad (3)$$

By taking the initial seed value, $\Theta = \pi$, and iteratively integrating over the entire collision path, the final angle of scatter for the projectile (Θ) can be evaluated in terms of the initial center of mass energy E_c, the interatomic potential V(r), and the impact parameter p. The impact or scattering parameter, p, is basically the effective interaction distance for "collision" between two atoms. Since the nuclei do not actually touch, the impact

parameter is defined as a circle of area πp^2 around the target nucleus. Any incident projectile that passes anywhere within this circle will be deflected by some angle greater than θ_c. The actual interaction distance during a collision depends on the energy of the collision. A useful frame of reference for describing collisional interaction distances is bounded by the Bohr radius (a_o = 0.053 nm) and the equilibrium separation, (r_o ~0.25 nm).

Since there is no single potential function that is appropriate for all pairs of ions and all energies, empirical parameters are usually fitted to pre-existing examples of interatomic potentials. Equation 4 describes the range of ions in terms of energy loss (or stopping power). The manner in which energetic particles interact with a lattice of stationary atoms can be described by the way the potential energy of a two-particle system varies with the distance between their centers. Ziegler, Biersack, and Littmark (ZBL) (1984) optimized a function originally developed by Lindhard, Scharff and Schiott (LSS) (1963). The result was a generalized analytical expression called the "Universal Screening Function" used to model interatomic potentials as given by equation 4 (Ziegler et al., 1984).

$$V(r) = \frac{Z_1 Z_2 e^2}{aR} \Phi(R) \tag{4}$$

In equation (4), Φ(R) is the universal screening function, R = r/a the reduced interatomic separation, Z_1 and Z_2 are the atomic numbers of the each of the two interacting species, and V(r) is the functional form of the interaction potential between the two atoms. The stopping power, S(E), is the average energy transferred when summed over all impact parameters as given in equation (5):

$$S(E) = \int_0^\infty T(E,p) 2\pi p dp = 2\pi\gamma E_o \int_0^{P_{\max}} \sin^2 \frac{\Theta}{2} p dp \tag{5}$$

where $\gamma \equiv \dfrac{4M_1M_2}{(M_1 + M_2)^2}$.

Thus, both the conservation of momentum and the interatomic potential are taken into account when the nuclear stopping power of an incident ion in a target material is considered.

2.2.3 Using TRIM for Monte Carlo Modeling of Ion - Solid Interactions in Amorphous Materials

Monte Carlo (MC) simulation of ion-solid interactions does have certain advantages over analytical formulations such as molecular dynamics (MD) calculations. MC methods allow more rigorous treatment of elastic scattering, and explicit consideration of surfaces and interfaces. Additionally, MC models allow energy and angular distributions to be readily determined. MC simulation methods rely on the statistical or random nature of the processes that are modeled. Energy transfer models of this sort are based on the linear superposition of sequential events or the random walk. The validity of the linear cascade approximation holds for cascade Regime II, when the number of moving atoms is small with respect to the total number of atoms contained within the collision volume.

As mentioned above, the nature of the collision cascade depends on M_1/M_2, and the incident ion energy. For a typical FIB application using a 5-50 keV Ga^+ ion beam, E_o is moderate, $M_1 \approx M_2$, and thus the conditions to produce a cascade characterized by linear collision dynamics are satisfied. Therefore, elastic energy losses can be assumed to be the result of a series of uncorrelated binary collisions and, the resulting phenomena can be readily modeled with MC computer simulation methods.

"Transport of Ions in Matter" (TRIM) is a sub-routine of a group of programs called "Stopping and Range of Ions in Matter" (SRIM) created by Ziegler et al. (1985, and Ziegler, 2003). TRIM can be effectively used to physically model the final 3D spatial distributions of ions in either simple or complex target materials. TRIM can generate data regarding the final 3D distributions of ions, as well as all kinetic data associated with the energy loss of the ion to the solid. For example, target damage, average sputtering yield per incident ion, ionization, and phonon production can all be quantitatively modeled using TRIM.

It should be noted that TRIM treats all targets as amorphous, thereby discarding the potential contribution of channeling or other orientation dependent phenomena to range distributions. This is an important consideration when attempting to correlate damage cascades with apparent damage layers that may develop during FIB milling of crystalline materials. TRIM was used to determine ranges for 100 Ga ions at different energies and incident angles for periodic table of elements (for solids) and are listed in the appendix.

With the strengths and the limitations of the SRIM package in mind, the code may be used to produce reasonable models of the variables that govern the FIB ion bombardment process. TRIM was used to physically model final 3D spatial distributions for 25 keV Ga^+ at 0^0 in elements Z = 3-84. The

range data was generated using the "Ion Distribution and Quick Calculation of Damage" option (Ziegler, 2003). This option allows the calculation to run more expeditiously by eliminating details about target damage or sputtering yields, while maintaining accurate results for the final distribution of ions in the solid.

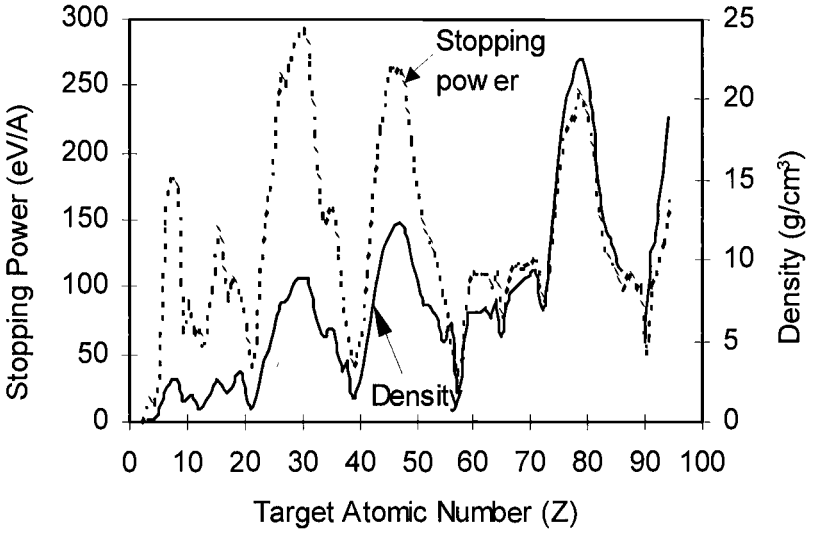

Figure 2-5. TRIM calculations showing the relationship between the total stopping power and the mass density for target elements Z= 1-92 at a Ga+ energy of 25 keV and 0° incident angle.

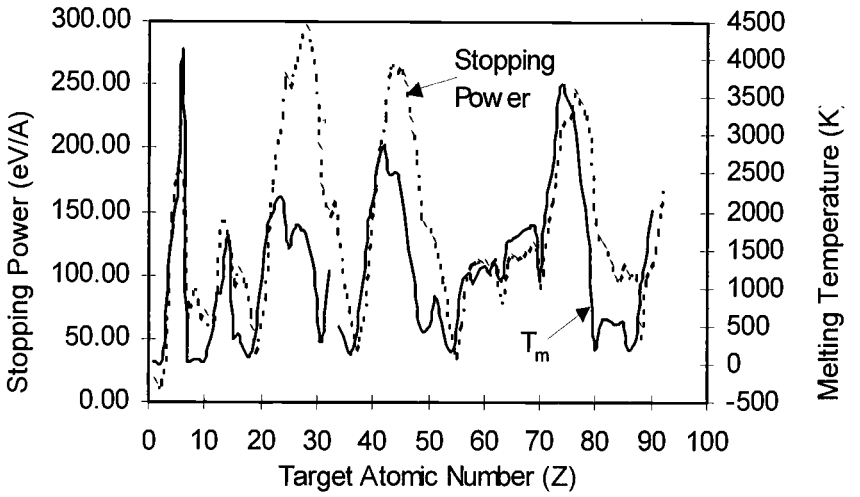

Figure 2-6. TRIM calculations showing the relationship between the total stopping power and the absolute melting temperature for target elements Z = 1-92 for a Ga+ beam at 25 keV and 0° incident angle.

The utility of such calculations can be extended by examining the periodic trends associated with S(E). Figures 5 and 6 show how the physical properties (i.e., melting temperature (T_m) and mass density (ρ_m)) of the elements compare with their corresponding stopping powers for a 25 keV Ga^+ beam at 0° incidence angle. Figure 5 shows a strong positive correlation between ρ_m and S(E). The position of the density and stopping power peaks are coincident for all the elements modeled. This illustrates that S(E) for each element follows the trends associated with its particular group when moving from left to right across the periodic table. In contrast, the magnitude of the individual S(E) peaks exhibit a nearly random distribution in height. This indicates the absence of periodic influence generally associated with increasing mass of the elements when moving from top to bottom within a group. There is an apparent anomaly observed in the peak heights among the elements Z = 58-71, which corresponds to the lanthanide series of elements. The diminished values observed for the physical properties among the lanthanide group are caused by population of the 4f shell in the absence of the covalent bonding contribution of the 5d shell. It is the covalent character of the d shells that imparts the exceptionally high strength of the interatomic bonding forces observed among the transition metals.

Figure 6 shows how stopping power compares with melting temperature for a 25 keV Ga^+ beam at 0° incidence angle. Similar to the example shown in Figure 5, there is also a strong positive correlation between T_m and S(E).

Collectively, the computer modeled data plotted in Figures 5 and 6 illustrates that stopping powers and associated range distributions strongly conform to the periodic trends associated with the electronic configuration of the elements across the periodic table, and to a lesser extent, to the trends associated with mass variations down a group. Thus, predictions with respect to anticipated implantation depth for a given target material may be made based on the position of the element in the periodic table.

2.3 Steady State Ion Implantation Conditions and the Concept of Ion Dose

Established terminology conventions used to describe the characteristics of an ion beam such as ion flux, fluence, dose, beam current, and current density have been used interchangeably and in some cases ambiguously in the literature. Many of the distinctions between the terms are subtle at best and warrant careful clarification. ***Flux*** is defined as the time rate of flow of energy; the radiant or luminous power in a beam. In the case of an ion beam flux is measured as the number of particles flowing through a given area per unit time and has units of ions/cm^2/s. Flux is a rate and remains constant for a given set of parameters such as beam current/aperture setting. (ASTM E1620-97). ***Fluence*** is, the sum of energies, the number of particles or photons incident during a given time interval on a small sphere centered at a given point in space divided by the cross-sectional area of that sphere. Fluence has units of ions/cm^2. Fluence is identical with the time integral of the particle flux density and thus, cumulatively increases as a function of the duration of the time interval that the beam is active (ANSI N1.1-1976). ***Dose*** is a general term denoting the quantity of radiation, energy, or particles absorbed by a medium. In the case of an ion beam, dose has units of ions/cm^2. Dose is the analogue of fluence with the distinction that fluence is the number of ions that pass through a defined area prior to impacting the target and dose is the number of ions that are impacted and absorbed into the target through a similarly defined area. Dose, like fluence, cumulatively increases as a function of the duration of the time interval that the beam is active. (ICRP 60-1990) Similar to flux, the ***beam current*** is also a measure of the time rate flow of energy or how many ions are delivered per unit time. The beam current is measured in amperes, which is equivalent to units of charge per unit time or Coulombs(C)/sec. In the case of a singly charged ion like Ga^+, the beam current can be described in terms of ions/s and is closely related to the flux, which is ions/cm^2/s, where the area is the cross-sectional

area of the beam. ***Current density*** is a measure of the energy intensity or number of ions in a given area at any instant in time. Current density has units of C/cm^2 or in the case of a singly charged ion like Ga^+ this is equivalent to $ions/cm^2$.

Although these conventions have origins in the ion implant community, it should be duly noted that certain aspects of the ion-solid interactions inherent to FIB processes are divergent from those that are characteristic of ion implantation. The major manifestation of these differences is seen in the dose i.e., the number of ions that are absorbed and retained in the target. FIB instruments typically operate in an energy range of 5-50 keV, whereas ion implantation is carried out over a broad array of energies that can range from tens of kilo-electron volts to several million electron volts. The energy of the incident beam and the atomic masses of the incident ions and target atoms govern the energy loss mechanisms operative in slowing and stopping the incident ions.

Ion implantation is performed in the energy regime where electronic stopping tends to dominate and sputtering is minimal. This is in contrast to FIB processes where the energy regime and masses are optimal for nuclear stopping which leads to efficient sputtering. Sputtering affects the implant profile as well as limiting the concentration of impurity atoms that can be implanted. As the target material is being bombarded with moderate energy ions, some of the incident beam ions are implanted and retained in the target while the surface that is exposed to the ion beam is simultaneously and constantly receding due to sputtering. FIB sputtering ultimately creates a steady-state condition between impurity implantation and impurity removal by sputtering. Once this steady state condition is reached, the concentration of impurity atoms reaches a maximum value. In general, the maximum concentration value (i.e., the steady-state condition) is attained after sputtering away a thickness comparable to the projected range. The concentration limit is proportional to the reciprocal of the sputtering yield, 1/Y. (Liau et al., 1980) Thus, a material that sputters very rapidly will have a lower peak impurity concentration than one with a correspondingly lower sputter yield.

In addition to the sputtering yield, the characteristics of the implanted impurity atoms also affect the implant profile and peak concentration. As impurity atoms are added to the solid, the attributes of the material are often altered. (Liau et al., 1980) This can lead to modification of the overall sputtering yield due to a change in the SBE and preferential sputtering where generally the ejection of light elements is favored. The preferential sputtering parameter, r, is essentially a ratio of the sputtering rate of the target to the sputtering rate of the impurity atoms. Since sputtering occurs from within the first few surface layers, preferential sputtering can lead to

significant variation in the maximum surface concentration of implanted atoms. Note that in contrast to FIB milling or other sputtering phenomena, ion implantation processes operate at very high beam energies and do not result in significant sputtering. Thus, during e.g., semiconductor ion implantation, an increase in ion implantation time (i.e., dose) corresponds to an increase in concentration, since steady state implantation conditions are not met. Ion implantation however, is a non-equilibrium process with the capability of producing materials with compositions unattainable by other conventional means. Thus, in FIB milling, an increase in dose does not alter the steady state equilibrium process of ion implantation, but rather, just increases the time in which the FIB milled surface will recede. Thus, in FIB milling, knowledge of dose may be useful for determining the depth of a receding surface, e.g., the depth of a FIB milled box cut.

In the absence of crystalline orientation effects and at low ion doses, the projected ion range distributions may be characterized by a simple Gaussian curve. However, as the dose increases (for a given beam energy), sputtering occurs and the depth distribution of implanted atoms typically has a maximum at the surface and falls off over a distance comparable to the initial ion range. This phenomenon is shown schematically in figure 7. Figure 7a shows the normalized ion concentration as a function of arbitrary distance units where no sputtering is observed (e.g., similar to that obtained via a simple TRIM calculation). Figure 7b shows an implanted ion concentration distribution as a function of distance once steady state sputtering conditions have been met.

It is therefore important to understand that simple generated TRIM collision cascades are statistical distributions of ion collisions and hence, does not account for steady state conditions between implantation and sputtering. The steady state surface composition for a single element target may be described by the following equation (Nastasi et al., 1996):

$$\frac{N_A}{N_B} = \frac{r}{(Y-1)} \tag{6}$$

In equation (6), N_A and N_B are the concentrations (per unit volume) of the implanted atom and the target atom respectively, r is a preferential sputtering factor (e.g., the ratio of the sputtering yield for a B atom to the sputtering yield for an A atom and is generally in the range of 0.5 to 2), and Y is the sputtering yield (Sigmund, 1991). At high doses, influences of preferential sputtering, segregation, atomic mixing, and chemical effects become important.

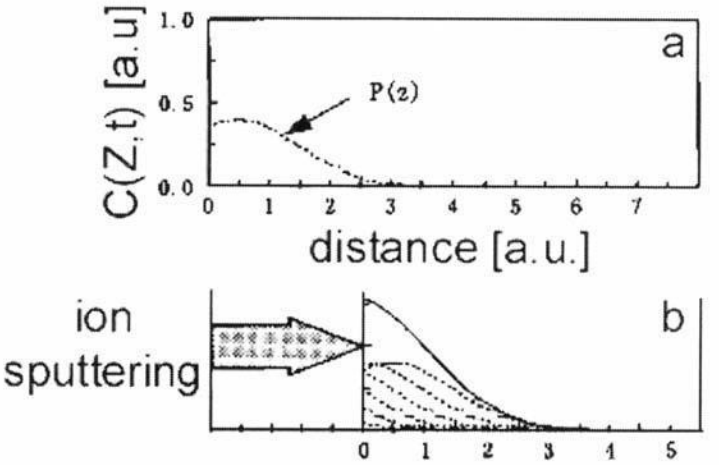

Figure 2-7. Schematic diagram of the implanted ion distribution once steady state sputtering is reached (figure obtained courtesy of Dr. T. Ishitani).

Implanted Ga concentrations of FIB prepared cross-sections in Si were estimated by Ishitani et al. (1998) to be 3.9 at % for r = 1, and 4.3 at % for r = 0.889, for a 30 keV Ga^+ beam at an incident angle of 87.5°. Since TEM specimens contain two surfaces that are FIB milled, they showed that a 50 nm thick TEM specimen would contain 1.3 at % Ga, while a 100 nm thick TEM specimen would contain 0.7 at % Ga.

3. SPUTTERING

The sputtering yield, Y, is defined as the number of ejected particles per incident ion. Sputtering can be considered as a statistical phenomena caused by surface erosion on an atomic scale. In this section we will discuss physical sputtering, whereby a transfer of kinetic energy from the incident ion to target atoms result in the ejection of surface and near surface atoms, also referred to as knock-on sputtering. Sputtering yields for typical FIB energies vary between $\sim 10^{-1} < Y < 10^{2}$ depending on target and incident angle (Andersen and Bay, 1981). Chemical sputtering will be discussed in the chapter on gas enhanced etching, where the physical sputtering rate may be enhanced by chemical reactions which produce an unstable compound with a diminished SBE at the target surface. The mean number of atoms ejected per incident ion with an energy exceeding some arbitrary minimum energy E_o may be expressed by equation (7) as

$$Y(E_o) \cong \frac{1}{4}\Gamma_m \frac{\alpha N S_n(E)\Delta x_o}{E_o} \quad (7)$$

where α is a dimensionless function incorporating the incidence angle, the mass ratio M_2/M_1, and the ion energy E, and Δx_o is the depth interval for which the atoms set in motion have an energy > E_o. (Sigmund, 1981). TRIM was used to determine the sputter yield for 100 Ga ions at different energies and incident angles for periodic table of elements (for solids). These values are listed in the appendix.

3.1 Ejection Direction During Sputtering

Sputtered particles generally possess an energy between ~ 2-5 eV. The emission of sputtered particles generally follows a cosine distribution for normal incidence ion bombardment (Behrisch, 1981). As the angle of incidence increases, the maximum emission of sputtered particles shifts away from the incoming ion beam as shown in figure 8.

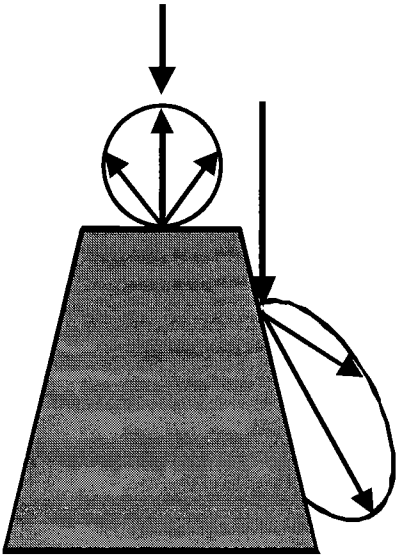

Figure 2-8. Schematic diagram of emission of sputtered particles with incident beam angle.

3.2 Backsputtering

Backsputtering occurs when an incident ion is scattered either directly, or after some number of multiple collisions, out of the target (Sigmund, 1981). (This phenomenon is analogous to backscattering in electron-solid interactions). As shown in figure 9 below, the backsputtering yield of the incident ion increases with angle of incidence. In addition, comparing the backsputtering yields between Si and Cu in figure 9 shows an increase in backsputtering with an increase in mass ratio M_2/M_1. Comparing figure 9 with the discussion on sputtering above, we see that in general, materials with a higher sputtering yield, have a correspondingly higher backsputtering yield of incident ions. Thus, more particles are available for the possibility of redeposition as will be discussed below. TRIM was used to determine the backsputter yield for 100 Ga ions at different energies and incident angles for periodic table of elements (for solids) and are listed in the appendix.

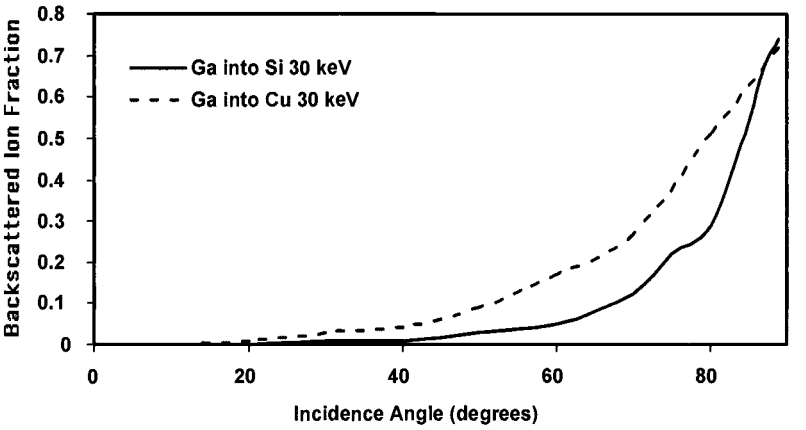

Figure 2-9. TRIM calculations showing backsputtering yield for Cu and Si as a function of incidence angle for 100 Ga ions at 30 keV.

4. REDEPOSITION

FIBs are most often used to create features of high aspect ratio (i.e., deep narrow trenches). Sputtered material and backsputtered ions may therefore deposit on surfaces that are in close proximity to the active milling site (e.g., the sidewalls of a deep narrow trench). Thus, surface degradation due to redeposition of sputtered material must also be considered during FIB milling. Controlling or at least predicting the manner in which redeposition of sputtered material will occur can be significant for the successful and rapid production of high quality TEM and other specimens by FIB techniques.

A hole milled with an FIB tends to be wide at the top surface and tapers down to a point at the bottom of the hole. The formation of this classic "V-shape" has been attributed to the redeposition of sputtered material that occurs when milling at high beam currents (Tartuani et al., 1993; Ishitani et al., 1994; Thayer, 1993; Yamaguchi et al., 1985; FEI, 1993; Walker, 1993). As the hole is made deeper, the effects of redeposition become increasingly severe until the rate of redeposition equals the rate of sputtering, thus limiting the aspect ratio of the milled hole. This effect of redeposition can be counteracted by the local introduction of a reactive gas species (i.e., Cl_2, I_2, and XeF_2) to the milling area (Thayer, 1993; FEI, 1993; Walker, 1993). The gas reacts with the sputtered material allowing it to be volatilized and removed by the vacuum system. Although reactive gas enhanced etching is an attractive solution to the problems resulting from redeposition, the gas has the potential to react with the sample material. The V-shaping that occurs in TEM specimens may be overcome by altering the angle of incidence with respect to the specimen surface for subsequent milling operations. The angle of incidence needed to prevent V-shaping is material dependent (e.g., it depends on the material sputtering rate). For example, while Si-based samples are generally tilted into the beam at 1-2°, it has been shown that a faster sputtering Zn sample must be tilted +/- 14° to create parallel sidewalls for TEM analysis (Prenitzer et al., 1998).

Redeposition is a function of a number of physically and chemically controlled variables, some of which include:

- The kinetic energy of the atoms leaving the surface
- The sticking coefficient of the target material
- The geometry of the feature being milled
- The sputtering yield (Y) of the target material

When an atom leaves a target material as a sputtered particle, it is ejected with a finite kinetic energy. A sputtered particle can, therefore, be considered a projectile capable of producing secondary interactions with local targets that lie in its trajectory. The direction and velocity of the ejected particle will be altered if it collides with another particle or the surface. Depending on the energy of impact and the sticking coefficient of the material, the sputtered atom may be redeposited on the surface that it strikes. The sticking coefficient is a statistical measure of a material's affinity to adhere to a surface, with a value of 1 equal to a 100% probability for sticking. It has been observed that there is very little difference in sticking probabilities for different materials for the low energy range exhibited by FIB sputtered particles (Andersen and Bay, 1981). However, it is shown below that the geometry of the feature to be milled and the sputtering yield play critical roles in the amount observed redeposition effects.

Figures 10a-c are SEM images of three trenches observed at a 70^{o} tilt. The trenches were all milled at normal incidence in (100) Si. A beam current of 1000 pA was used to deliver a variable but known fluence per unit area to the three trenches. The doses were varied by controlling the scan time of the beam. The trench in figure 10a received a fluence of 1.5×10^{12} Ga^{+} ions in 4 minutes, the trench in figure 10b received a fluence of 3.0×10^{12} Ga^{+} ions in 8 minutes, and the trench in figure 10c received a fluence of 6.0×10^{12} Ga^{+} ions in 16 minutes. The series of doses allows the progression of milling to be followed in time. The images provide evidence suggesting an increase in redeposition as the aspect ratio is increased. The shallowest trench has a fairly smooth appearance on the sidewalls and bottom. The sidewalls are still relatively vertical although they are somewhat rounded at the top. The second trench is beginning to show some roughening of the sidewalls and corners which is consistent with the appearance of redeposited material. Also, the sidewalls are beginning to show a greater deviation from the vertical direction. The third case clearly shows the effects of redeposition. The sidewalls have roughened considerably and the shape conforms to a definitive "V".

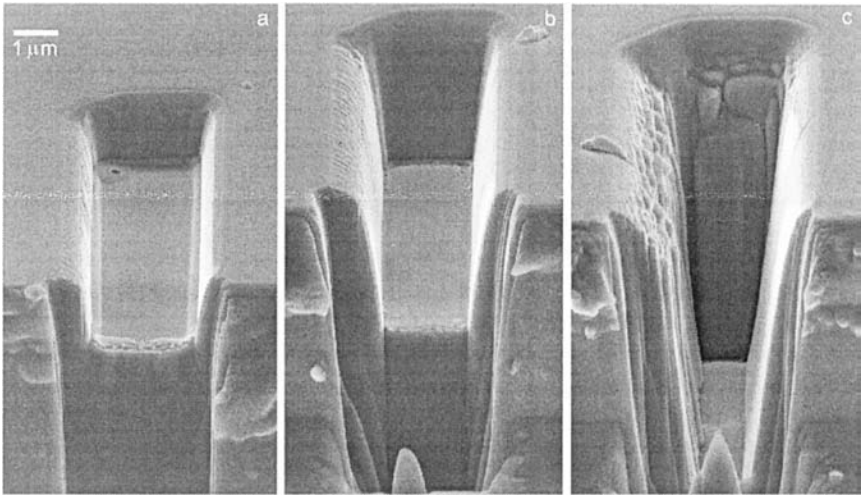

Figure 2-10. Rectangular FIB trenches in (100) Si milled at normal incidence by applying: (a) single fluence, (b) double fluence, and (c) triple fluence of Ga^+ ions at 25 keV.

An increased pressure mechanism for redeposition was proposed by Prenitzer (1999) where it was observed that both the degree to which the sputtered material is restricted from escaping the confines of the trench and the rate at which material is removed from the target have a profound effect on the observed degree of redeposition. Confining trench geometry such as large aspect ratios as well as factors that enhance the kinetics of material removal will tend to increase problems associated with redeposition.

It is important to make a distinction between sputtering rate (Y_t) and sputtering yield, Y. Y can be interpreted as the average number of target atoms ejected from the sample per incident ion. Y is an event dependent measure of the material removal. Y_t is the number of atoms being sputtered from the target per unit time. Therefore, Y_t is the actual time dependent, kinetic material removal parameter. A reasonable estimate of Y_t can be made by multiplying Y by the beam current, (i.e., the rate of delivery of ions to the target surface).

The mechanism that is proposed below to explain the "Classic V Shape" can be instructive in illustrating how the observed limits on aspect ratios attainable by FIB milling are influenced by both kinetic factors and trench geometry. When milling a trench, the rate of material removal can be considered to be in dynamic equilibrium with the rate of redeposition. For redeposition to occur atoms must be ejected from the target material with enough kinetic energy to carry them to a proximal surface with which they may collide and stick. In order to show how factors that enhance Y_t also

enhance redeposition related problems, Y_t must be considered in terms of the effect it exerts on its surroundings. The rate of material removal from the target material equals the rate of atoms introduced into the vacuum chamber. Thus, the rate of redeposition is ultimately a function of the dynamic equilibrium between Y_t and the capacity of the vacuum system to remove the sputtered atoms from the chamber. If the vacuum system is able to evacuate the sputtered material at a rate which is greater than or equal to Y_t, theoretically there can be no redeposition because there will be no free atoms.

As an illustrative example, a nominal sputtering yield of 10 and a beam current of 2000 pA equates to the beam delivering ~1.2 x 10^{10} Ga^+ ions per second with each ion resulting in the sputtering of 10 target atoms. Thus, 1.2 x 10^{11} target atoms are introduced into the chamber per second (neglecting any contributions from backsputtering). We assume that the volume of a typical FIB specimen chamber is on the order of 70 L. If the ideal gas law is assumed to apply within the chamber where the vacuum is better than 10^{-7} torr, then it can be shown that one could sputter at this rate for 18 days before the pressure was increased by one order of magnitude.

Recalling the proposed mechanism for the "Classic V Shape:" as a trench deepens, the confining geometry restricts the escape of sputtered material. Thus, even though the overall pressure may be completely unaffected by sputtering, it can be shown that localized pressures in a typical trench of nominal dimensions 20 μm x 10 μm x 5 μm can rise at an estimated 393 torr/sec by the introduction of 10^{10} particles per second.

Thus, as the localized pressure increases, the collisional mean free path between particles in the confined region is reduced and may be expressed by equation (8):

$$\lambda = \frac{1}{\sqrt{2}d^2(p/kT)} \tag{8}$$

where λ is the mean free path, d is the collision parameter, p is the pressure in atm, T is the absolute temperature, and k is Boltzman's constant (1.38×10^{-23} J/K).

Therefore, for T = 298K and d = 0.25 nm, the mean free path between collisions for particles in a trench can be expected to decrease by ~10 orders of magnitude when the localized pressure increases by 2 orders of magnitude as predicted above. In summary, as Y_t increases, the localized pressure within the confines of a trench increases. This causes a significant decrease in the collisional mean free path of the sputtered atoms within the trench. Thus, the probability of sample/sputtered atom collisions resulting in redeposition increases as Y_t increases. For a fixed set of FIB and target

parameters, redeposition artifacts are observed for smaller trenches. For a constant trench size and holding all other FIB parameters constant, redeposition artifacts would increase for either (i) a target with a larger sputtering yield, (ii) increasing the material sputtering yield via a change in incidence angle or beam energy, or (iii), increasing the beam current.

4.1 Effect of Collision Cascade on Sputtering Yield

In order to model sputtering behavior, both the incident ion and the recoil atoms are followed throughout the deceleration process in 3D until their energy falls below a predetermined level. The minimum energy is usually set to < 5 eV for the incident ion, and a value that is less than the SBE of the target material for the knock-on atoms. The SBE is usually approximated by the heat of sublimation. Once a recoil atom moves into a position outside the target surface it is considered a candidate for sputtering. If its energy component normal to the surface is great enough to overcome its SBE, it is registered along with its emission angle as a sputtered particle. If it the energy component is less than its SBE, the atom is registered as being reflected back into the sample and is tracked through further collisions. TRIM may be used to quantify the average sputtering yield for an incident ion (Ziegler, 2003).

TRIM was used to determine the projected range and sputtering yield for 500 Ga ions at 30 keV for Si and Cu at 0° and 89° incident angle and at 5 keV for Si and Cu at 0° and 85° incident angle. The TRIM plots for these conditions are shown in figure 11 and figure 12 respectively, where the full scale for the ion trajectories is 50 nm (500 Å). The sputtering yield is noted in the lower right hand corner of each image.

Sputtering is a surface phenomenon. It is only the collision cascade atoms that are in motion near the target surface that have the potential to cause an atom to be ejected as a sputtered particle. Thus from a statistical perspective, the more collisions that take place proximal to the surface, the higher the sputtering yield will be. The position of the cascade is determined by the nuclear stopping power of an ion in a given target material and the incident angle of the beam with respect to the target surface. This is illustrated in figures 11 and 12, where the ion trajectories for the Cu are observed to be closer to the surface than the ion trajectories for Si at the same energy and incidence angle. The sputter yield for Cu is

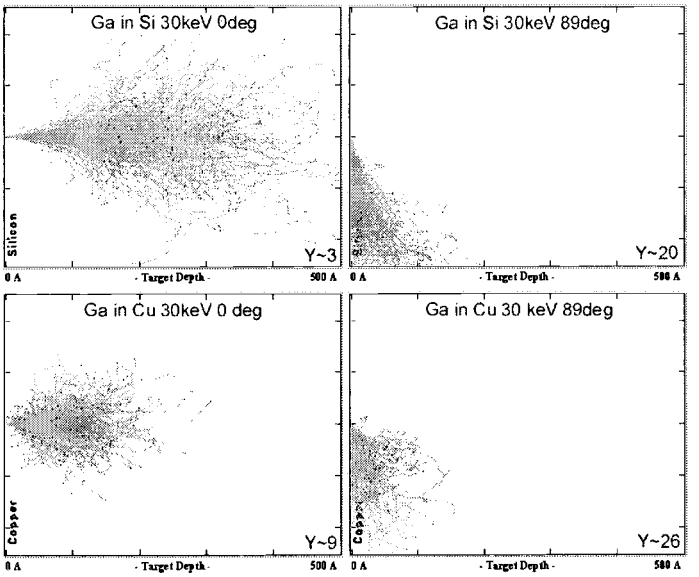

Figure 2-11. TRIM ion trajectories for 500 30 keV Ga^+ ions in Si and Cu and 0° and 89°.

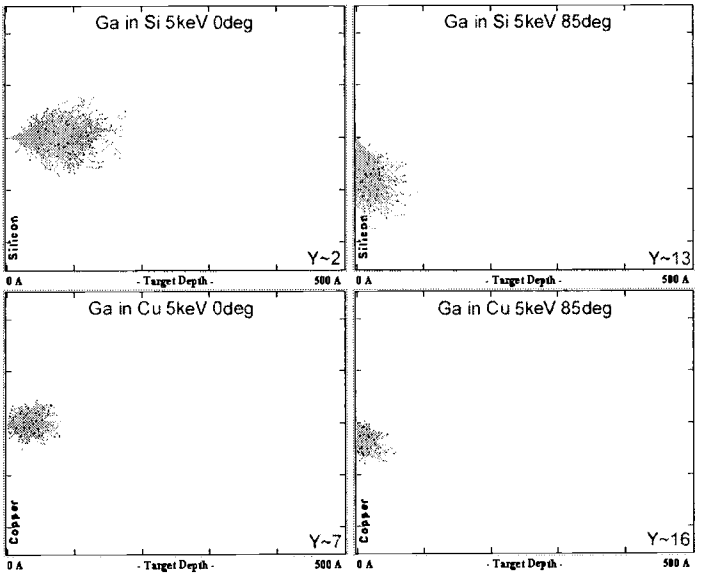

Figure 2-12. TRIM ion trajectories for 500 5 keV Ga^+ ions in Si and Cu and 0° and 85°.

correspondingly higher than that for Si at each incident angle shown. It should be noted that the relative difference in sputtering yield between the two materials is disproportionate to the relative difference in their melting temperatures. Furthermore, the difference in sputtering yield between the two materials decreases as the angle of incidence increases. This indicates that although the dominant mechanism controlling sputter yield is bond strength or SBE, the position of the collision cascade is also significant and may be more of an influence at greater incident angles.

Figure 13 shows how the sputter yield varies as a function of energy for Cu and Si at two different incident angles. The energy range modeled between 5-30 keV is within the nuclear stopping range for this system. The graph shows that the sputtering yield increases steadily with an increase in accelerating voltage at an incident angle of 89°. At the higher incident angle the collision cascade is confined in a region close to the surface. Thus, an increase in accelerating voltage would statistically result in an increase in the number of surface collisions with enough energy to overcome the SBE and consequently increase the sputtering yield. When the beam is at normal incidence with respect to the target surface an increase in accelerating voltage would also statistically result in an increase in the number of collisions cascade atoms with enough energy to overcome the SBE; however, at normal incidence the predominant effect of an increase in the accelerating voltage would be an increased projected range. Thus, the collision cascade would be located deeper under the surface of the target, subsequently mediating the effect of the increased energy of the cascade atoms. The result is a less dramatic increase in sputter yield with an increase in accelerating voltage at normal incidence. This is particularly evident in the Si target where the relatively low stopping power is not as effective at confining the collision cascade relative to Cu.

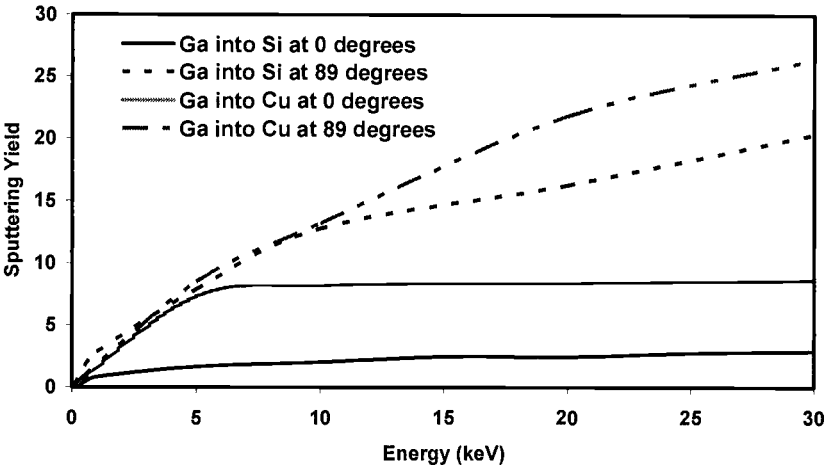

Figure 2-13. TRIM sputtering yields for 30 keV Ga+ ions into Si and Cu.

4.2 Dependence of Sputtering Yield on Target Material and Incident Angle

Figure 14 shows the effects of incidence angle on the sputtering yield for Si and Cu at 30 keV. Note that Y increases to a maximum and then approaches zero for increasing angle of incidence. This maximum sputtering yield occurs between ~ 75-85° depending in the material. It is interesting to note that early uses of broad beam Ar ion milling for TEM specimen preparation were generally performed at these angles of largest sputtering yield. The work pioneered by Barna et al. (1990) soon showed that these large sputtering yield angles were the worst possible angles in which to prepare thin specimens due to the large topography (i.e., "pillows") that developed on these surfaces. Barna's work showed that the best TEM specimens were obtained when ion milled at glancing angles with respect to the sample surface and at the lowest energy possible, thereby, producing a flat and polished surface. These are the same glancing angles (i.e., ~ 89°) that are now routinely used in FIB specimen preparation. The broad beam Ar ion mill is now routinely used after FIB milling to replace FIB damage

with a smaller amount of Ar milling damage (see discussion on FIB damage elsewhere in this volume).

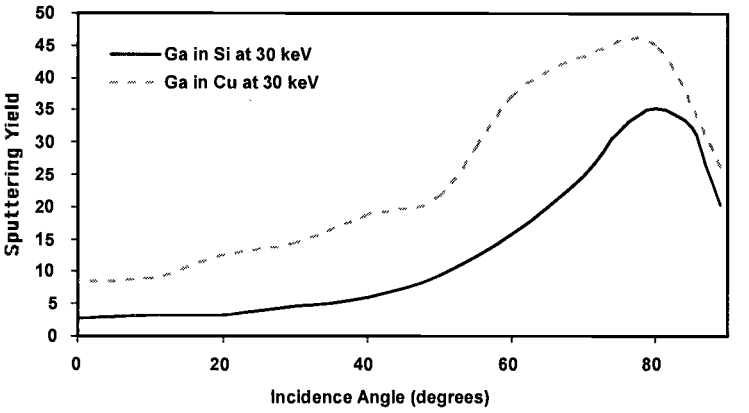

Fi

Figure 2-14. Sputtering yield as a function of incidence angle for 30 keV Ga^+ in Si and Cu.

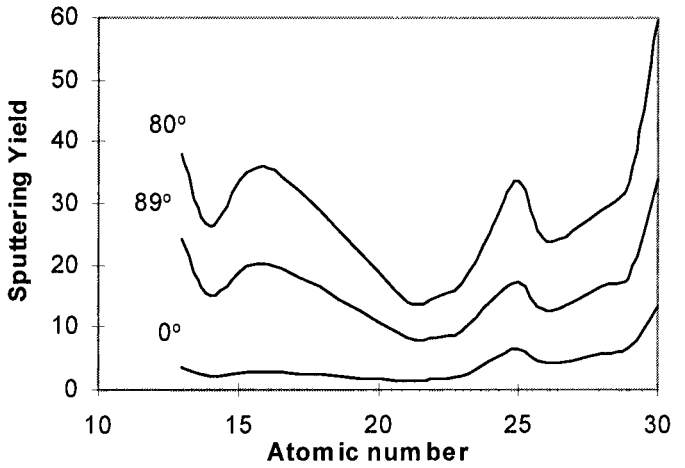

Figure 2-15. Material dependence of sputtering yield for materials Z = 13-30 at various angles of incidence from normal for 25 keV Ga+. (Data modeled with TRIM'97).

The material dependence of sputtering yield (Y(Z)) for a given set of milling parameters is illustrated in figure 15. The results of detailed calculations with full damage cascades modeled with TRIM for target materials, Z = 13-30 bombarded with 25 keV Ga^+ are shown in Figure 15 (and refer back to figures 11,12,13).

Figure 15 shows how the sputtering yield varies for different elements. The position of the peaks and valleys with respect to the x-axis indicates that periodic trends, associated with electronic structure of the elements, exert a controlling influence on the sputtering yield. The positions of corresponding peaks among the three data sets are invariant with respect to the incident milling angle. This suggests that Y(Z) remains consistent while the angular orientation between the target and the beam is varied. Thus, a material with a high relative Y(Z) will mill rapidly at any incident angle. As discussed in section 4.2, this indicates a physical rather than a chemical control mechanism for the angular variance of Y. Although the shapes of the three curves mimic one other, they are not coincident. The relative position of each curve with respect to the y-axis indicates the sputtering efficiency associated with that particular incident angle $Y(\theta)$ as also shown in figure 13. There is also some deviation between the magnitudes of corresponding peaks with incident angle. This is also consistent with the data shown in figure 13.

Figures 16a-d are SEM images of trenches milled with a 1000 pA beam at the same fluence into Zn, Cu, Al, and Si, respectively. The images provide a clear example of how different materials behave uniquely under the influence of the ion beam. Relative trench depths are a good indicator of relative Y(Z) with the incident angle, beam current, milling time, and accelerating voltage held constant. The relative depth of the trenches in Figures 16a-d yields a qualitative measure of the volume of material removed for a given ion fluence. It should be noted that this experiment is not intended to be presented as a rigorous quantification of Y(Z), but rather as an generalization to demonstrate the relative periodic behavior of Y(Z) for various materials.

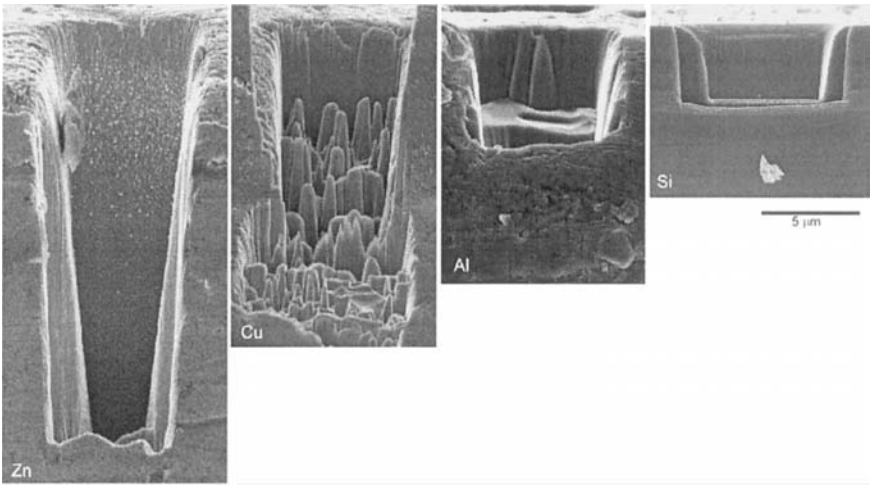

Figure 2-16. SEM images of cross-sectioned FIB trenches milled at 25 keV and constant fluence for Zn, Cu, Al, and Si.

Figure 16a is the trench milled in Zn. The Zn trench is the deepest which is consistent with the theoretical prediction that Zn will mill the fastest of the four materials shown at Y(Zn) = 12.9 atoms/25 keV Ga^+ ion. The Zn also shows the most severe sloping of the sidewalls. This is expected behavior based on the concepts developed to explain redeposition as previously explained. Figure 16b shows a trench milled in Cu. The relative trench depth of Cu is also in agreement with the predicted relative Y(Cu) = 7.0 atoms/Ga^+ ion. Figure 16c shows that the Al does not show roughening under ion bombardment at normal incidence. The trench floor and sidewalls are relatively smooth having a minimum of discontinuities. The relative depth is in accordance with the modeled Y(Al) = 3.5 atoms/Ga^+ ion. Figure 16d is the trench milled into Si. Of the four materials shown, the Si appears to show the least amount of milling induced topography. The Si trench sidewalls and bottom are relatively uniform, and excluding the non-vertical sidewalls, the trench appears virtually free from the effects of redeposition as observed by SEM. The relative trench depth observed in Si also conforms to the predicted relative Y(Si) = 2.1 atoms/ Ga^+ ion.

The periodic fluctuations in sputtering yield demonstrated in the previous section are manifestations of the influence that the interatomic potential exerts on the physical properties of a given material. Thus, range data and sputtering yields predicted by computer modeling, as well as the supporting empirical results show that material dependent properties of a solid are governed by the forces that bind the constituent atoms together.

When the data described above are combined with some other well-established periodic trends, such as T_m as shown in Figure 17, it becomes evident that there are very useful correlations to be formulated. Sputtering yield exhibits an inverse correlation with T_m. This type of relationship is intuitive since T_m is direct indicator of bond strength. The more tightly bound an atom is, the more difficult it will be to eject it as a sputtered particle.

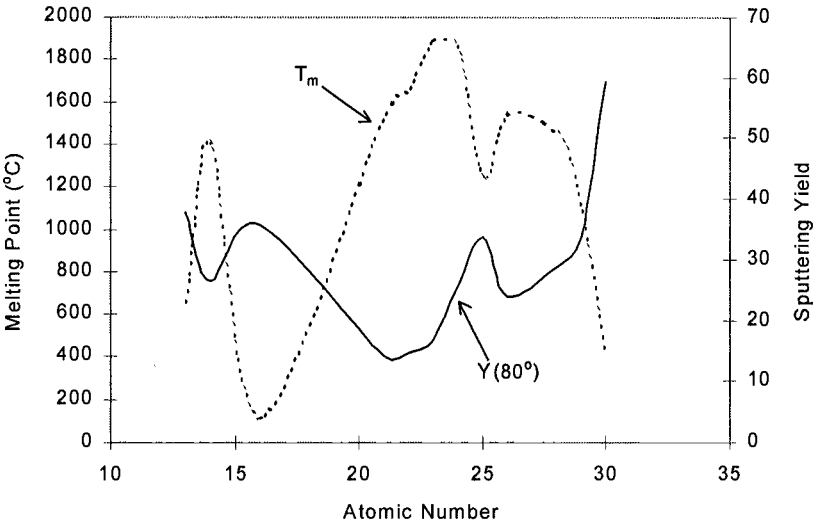

Figure 2-17. The correlation between sputtering yield at 80° angle of incidence and melting temperature for elements, Z = 13 through 30 and a 25 keV Ga+ beam (Data modeled with TRIM'97).

It has been established that material dependent milling induced behavior is influenced by the same interatomic forces that govern other periodic behaviors of the elements. Therefore, phenomena such as sputtering yields and range distributions can themselves be regarded as periodic properties of the elements. This allows the familiar and available periodic table to be used as a tool for predicting milling behavior. Predictions of how an unfamiliar material may respond to Ga^+ milling has many practical implications for FIB applications.

4.3 Ion Channeling

In the discussion of range, stopping power, and sputtering behavior above, it was assumed that the target was disordered, i.e., amorphous. It was observed that the factors that affect sputtering include the atomic number (i.e., mass), energy, and angle of incidence of the ion beam, the mass of the target, and the SBE of the target. The phenomenon of ion channeling occurs in crystalline materials. Channeling is a process whereby ions may penetrate greater distances along low index directions compared to non-channeling directions or amorphous materials. Channeling thereby increases the range of ions, moving the collision cascade further from the surface. Since channeling influences the ion range (i.e., the shape of the collision cascade), it also has dramatic affects on image contrast, damage depths, and sputtering yields.

Ion channeling is responsible for the varying contrast in secondary electron images for polycrystalline samples (Franklin et al., 1988; Kola et al., 1993). Channeling contrast results because the secondary electron yield varies as a function of crystallographic orientation within the sample. Thus, a single crystal region (i.e., a grain in a polycrystalline sample) will appear darker when it is aligned (or nearly aligned) to a low index direction due to a decrease in the number of emitted secondary electrons. Figure 18 below shows an example of the dramatic channeling contrast observed for a polycrystalline Cu specimen. There are many other examples of images showing channeling contrast in this volume.

Ion channeling will also decrease the sputtering yield of a material, the physics and mathematics of which may be found elsewhere (Lindhard, 1964; Onderdelinden, 1966; Sprague et al., 1987; W. Palmer et al., 1990; Hosler et al., 1993). Figure 19 shows secondary electron FIB image of FIB milled trenches in a Cu bicrystal showing differences in sputtering yield with channeling effects (Kempshall et al. 2001). The interesting feature to note in Figure 19 is the correlation between the ion channeling contrast and the milling characteristics. When a grain is oriented to the [100] channeling direction, the milling characteristics of the Cu improve as evident by the flat trench bottoms and clean trench walls. Conversely, the trench milled in the grain that is not aligned with the [100] direction has poor milling characteristics as evident by the rough trench bottom and the sloped trench wall, which is consistent with redeposition effects via an increase in sputtering rate as described above. Furthermore, it is clearly evident by the differing depths in the 24 μm x 2 μm trench that the non-channeled side of the trench mills quicker than the channeled side of the trench. Since the ion channeling contrast has been shown to be directly proportional to the sputtering yield, the differences in milling characteristics can be accounted

for by looking at the mechanism that affects both the contrast and the sputtering yield, specifically, channeling. Figure 19 also shows how channeling affects both image contrast (i.e., the generation of secondary electrons) as well as sputtering yield. Figure 20 shows a secondary electron FIB image of the UCF pegasus logo FIB milled into adjacent grains of a 10^{o}/[100] twist boundary. Note that the right grain is aligned to the [100] direction and shows dark contrast, while the left grain oriented 10^{o} from [100] shows bright contrast. The faster sputtering left grain also shows enhanced redeposition artifacts on the sidewalls of the cuts, again showing the relationship between sputtering rate and redeposition artifacts.

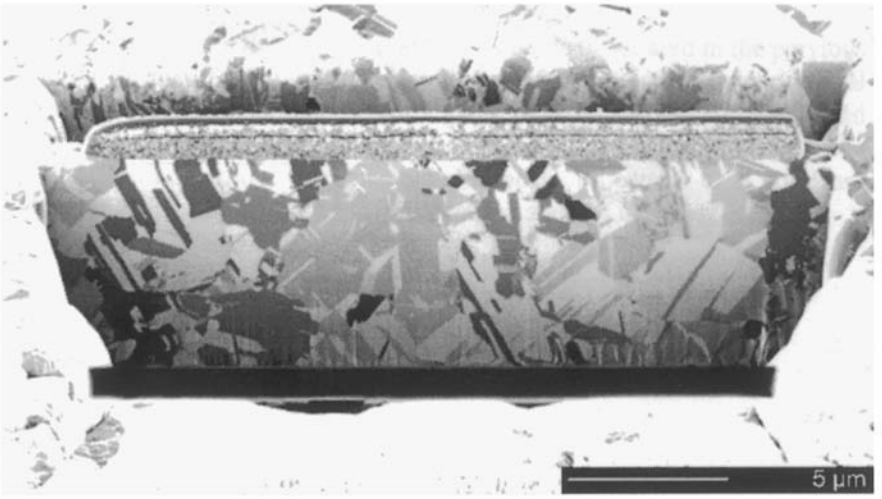

Figure 2-18. An ion induced secondary electron image illustrating channeling contrast in a FIB polished polycrystalline Cu sample (sample courtesy of S. Merchant).

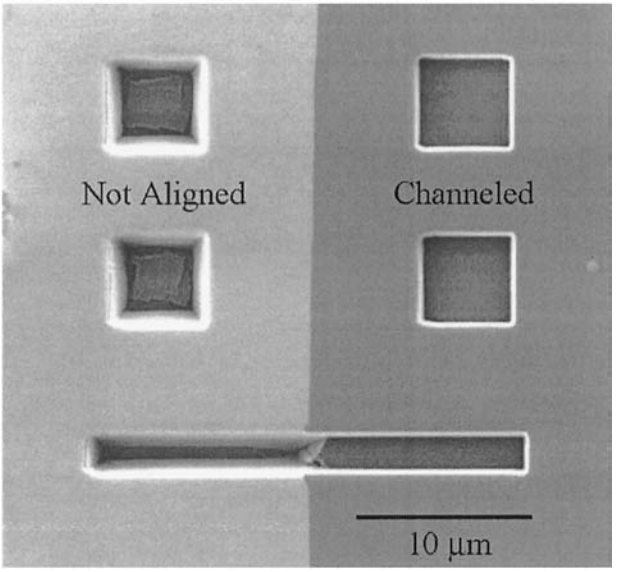

Figure 2-19. Secondary electron FIB image of milled trenches in a Cu bicrystal indicating differences in sputtering yield with channeling effects.

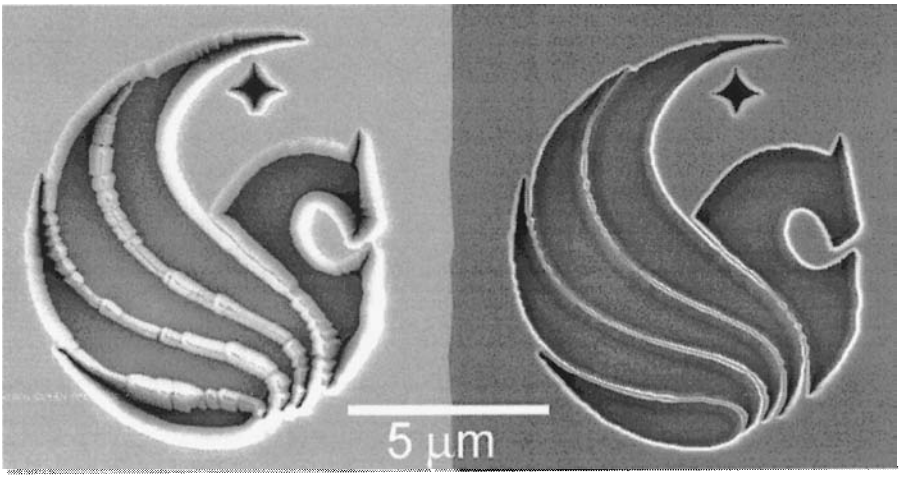

Figure 2-20. A secondary electron FIB image of the UCF pegasus logo FIB milled into adjacent grains separated by a 10°/[100] twist boundary.

The relative channeling contrast that is observed from one material to the next depends mainly on the interatomic planar distances, the atomic density of the target material, and the Thomas-Fermi screening length. In the case of using 30keV Ga^+ as the incident ion, ion channeling is significant for materials that have close packed crystal structures with higher atomic densities like Al, Cu, Ni, and Au and less significant for materials that have lower atomic densities like Si. As a result, the amount of ion channeling contrast, and hence, differential sputtering observed for a material like Cu is significant, while Si tends to not yield a readily observable amount of ion channeling contrast or differential sputtering.

5. ION IRRADIATION DAMAGE IN MATERIALS

5.1 Amorphization

An inherent ion-solid interaction in the FIB process is the result of ion implantation into the target surface. The degree of ion implantation depends on ion energy, angle of incidence, ion species, and target material as discussed above. Sample preparation by FIB uses the process of ion bombardment to selectively remove material. Atoms that are displaced from their equilibrium positions by the impingement of energetic ions generate a collision cascade within the target material. Sputtering occurs if sufficient momentum is transferred to a surface atom. One consequence of ion implantation can be the development of a surface amorphous phase. The amorphous phase induced in crystalline materials by ion bombardment is typically metastable, and its formation depends on unit cell size, complexity of chemical ordering, and the width of an intermetallic phase field (Nastasi, 24). The restoration of the collision cascade induced disorder requires correlated and cooperative motion of alloying atoms. The more complex the material unit cell, the larger the amorphous layer will be. Likewise, smaller unit-celled materials are difficult to amorphize. Additionally, alloys or materials with a broad phase field will remain crystalline, since the atomic packing arrangement is less stringent than line compounds or stochiometric intermetallics. Consistent with the discussion above, we have observed that Si amorphizes when FIB milled, while Cu does not (Matteson et al., 2002). It should be noted that Cu has been observed to form a Cu_3Ga phase when FIB milled at certain crystallographic directions (see chapter by Phaneuf in this volume).

5.2 Local Heating in FIB Milled Surfaces?

Averbeck et al. (1994) have used molecular dynamics simulations to investigate the collision cascade during ion bombardment in crystalline materials. An example of a 10 keV Au particle impinging on a (100) Au surface is shown in figure 21. At the onset of particle bombardment (figure 21a), displaced atoms are observed within the collision cascade. After ~ 1ps (figure 21b), the atoms in the collision cascade are in such disorder that they may be considered to be a liquid. This disorder continues through to ~ 4ps (figure 21c). However, between ~ 10 ps (figure 21d) to ~ 20 ps (figure 21e), the atoms in the collision cascade begin to relax or "self anneal" back into their equilibrium lattice positions. The entire process is over within ~ 30 ps (figure 21f) and the atomic region that included the collision cascade is shown to consist of crystalline point defects. Thus, for the simple centered-close-packed Au structure, ion bombardment results in the generation of crystalline defects. In addition, local heating by the FIB process is restricted to the region defined by the collision cascade. Since the small FIB beam must be rastered over an area in order for milling to occur (contrary to broad beam ion milling where a sample region may experience constant bombardment by the impinging ions), where the beam dwell times are on the order of micro-seconds, heating effects for most materials may be deemed to be negligible. In our lab, we have only observed one case in a proprietary polymeric material where beam damage was so extensive that a thin TEM membrane could not be prepared. *Thus, any specimen "heating" due to FIB milling will be confined to the collision cascade which is on the order of a few tens of nanometers or less for most materials.*

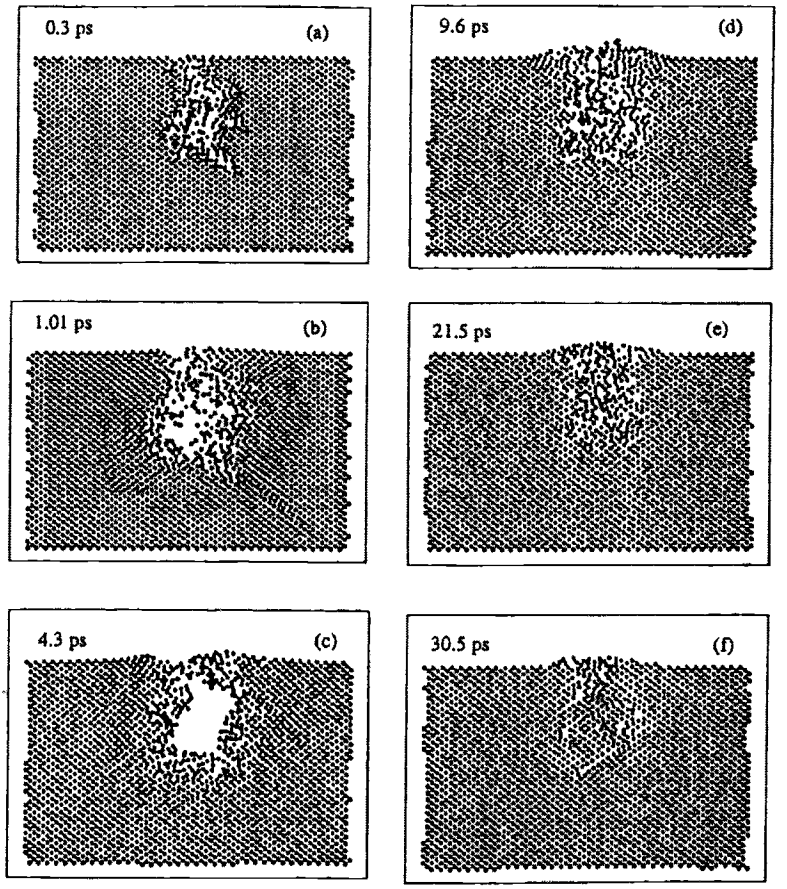

Figure 2-21. MD simulation of a 10 keV Au particle on a (100) Au surface (Averbeck et al., 1994, used with permission, Journal of Applied Physics, © American Institute of Physics)

5.3 Amorphization vs. Redeposition

There seems to be some disparity in the literature as to how much Ga is actually implanted in materials, and how much amorphization damage is expected to occur in certain materials. There is a distinct difference between damage due to inherent ion-solid interactions and redeposition artifacts (Rajsiri et al., 2002). FIB milled side-walls in Si were cross-sectioned using the FIB in-situ lift-out technique as described elsewhere in this volume. As shown by figure 22, the damage along the side-wall actually consists of two distinct regions. The bright contrast region adjacent to the single crystal Si

shows ~ 20 nm of amorphization damage. Between the amorphization region and a protective Cr layer is a region of darker contrast (~ 50 nm). XEDS spectra obtained from the dark region shows large amounts of Ga (~37 wt % or ~ 15 at %) in Si. As shown by figure 22, ~70% of the incident Ga^+ ions may be backsputtered during FIB milling at the large incident angles used FIB milling sidewalls. This dark region in the bright field TEM image is consistent with mass/thickness contrast and thus clearly indicates a redeposition layer containing sputtered Si and Ga plus backsputtered Ga.

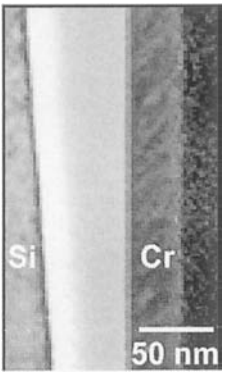

Figure 2-22. Cross-section TEM image of the side-wall of Si FIB milled with 30 keV Ga^+ ions at 1000pA showing an amorphization region and a redeposition region.

If a simple case is considered where 100 Ga^+ ions bombard a Si surface at 89° and 30 keV, then 70 ions will be backsputtered, and the remaining 30 ions will produce ~ 600 sputtered Si atoms. Assuming that no backsputtered ions will contribute to the Si sputter yield, and neglecting that steady state sputtering also removes implanted Ga ions, then ~ 10 at % Ga will be available in the sputtered material. Thus, the ~ 15 at % Ga that is observed in the redeposition region is consistent with the amount of Ga that is also available in the sputtered particles in this simple comparison.

The amorphization layer yielded ~ 0.4 wt % Ga (0.16 at %) within this region. XEDS results obtained from the Si just below the amorphization region showed ~0.1 wt % Ga. This implies that the amount of Ga implanted into the crystalline Si is on the order of the resolution of the XEDS technique. These results are also less than that predicted by Ishitani et al. discussed in section 1.3 above, although the differences may be explained due to differences in incident angles. The importance of these results is that any significant amount of Ga observed in FIB milled Si (i.e., > 1 wt %) is due to redeposition artifacts and not due to inherent ion-solid interactions.

6. SUMMARY

The basics of ion-solid interactions particular to FIB milling have been presented. The concepts and methods to model ion range, sputtering, and ion irradiation damage have been reviewed. It was shown that materials subjected to bombardment by energetic ions tend to exhibit microstructural and topographical disruption. The response of a given target material to the ion beam is strongly dependent on factors such as beam current, incident ion energy, trench/feature geometry, raster pattern, and milling angle. Many of the artifacts that are typically associated with FIB prepared TEM specimens are due to redeposition and not to inherent ion-solid interactions. Problems associated with redeposition (i.e., exaggerated sidewall sloping, formation of undesired topography, or the inclusion of high levels of Ga^+ in the specimen) are controllable. Redeposition is enhanced by factors that increase the rate of sputtering and/or restrict the removal of the sputtered material from the active milling site. The sputtering rate is increased by increasing the beam current, and/or changing parameters that increase the sputtering yield (e.g., milling at an incident angle of ~80°, milling a material with an inherently high sputtering yield, or crystallographic effects). The removal of sputtered material from the active milling site is particularly impeded when milling high aspect ratio trenches. Redeposition related artifacts may be minimized by understanding and selecting appropriate combinations of the milling parameters (e.g., reducing the beam current when milling a material with an inherently high sputtering yield).

Material inherent properties such as sputtering yield or stopping power are dictated by the same interatomic forces that govern other periodic behaviors of the elements. Therefore, phenomena such as sputtering yield and range distributions can themselves be regarded as periodic properties of the elements. This allows the familiar periodic table to be used as a tool for predicting milling behavior.

The objective of the FIB LO method is to rapidly produce a high quality electron transparent membrane to be imaged in the TEM. Because a TEM specimen must be representative of the bulk microstructure, any modifications that the specimen might incur during the preparation process must be well characterized. An understanding of the fundamental ion/solid interactions that govern the milling process as outlined above insures the accuracy of the information obtained from an FIB prepared TEM specimen. Such an understanding of ion/solid interactions can also be used to predict milling behavior of novel materials, improve overall specimen quality and increase the success rates for FIB EM specimen preparation.

ACKNOWLEDGEMENTS

The authors would like to thank the I4/UCF/Cirent/Agere Partnership, NSF DMR #9703281, AMPAC, Florida Space Grant Consortium, Florida Solar Energy Center, and the DOE OIT program for financial support. Special thanks to Jeff Bindell for his undying support of the UCF/Cirent/Agere partnership.

REFERENCES

American Society for Testing and Materials. E1620-97, "Standard Terminology Relating to Liquid Particles and Atomization," in Annual Book of ASTM Standards v. 14.02 General Test Methods; Forensic Sciences; Terminology; Conformity Assessment; Statistical Methods, ASTM International, West Conshohocken, PA, v.14.02 (1997)

Andersen HH and Bay HL, "Sputtering Yield Measurements," in Sputtering by Particle Bombardment I, Physical Sputtering of Single-Element Solids, ed. R Behrisch, Springer Verlag, Berlin, 145-218 (1981).

ANSI N1.1-1976, American National Standards Glossary of Terms in Nuclear Science and Technology, American National Standards Institute New York, NY (1976)

Averbeck RS, Ghaly M, "A Model for Surface Damage in Ion-Irradiated Solids," Journal of Applied Physics, 76, 6, 3908 (1994).

Barna A, Barna, PB, Zalar A, "Ion Beam induced roughness and its effect in AES depth profiling of multilayer Ni/Cr thin films," Surface and Interface Analysis, 12 1-2, 144-150 (1988).

Barna A and Barna PB, Zalar, A, "Analysis of the development of large area surface topography during ion etching," Vacuum, 40, 1-2, 115-120 (1990).

Behrisch R, "Introduction and Overview," in Sputtering by Particle Bombardment I, Physical Sputtering of Single-Element Solids, ed. R Behrisch, Springer Verlag, Berlin, 1-8. (1981).

FEI Focused Ion Beam Application Note, "High Aspect Ratio Hole Drilling Using FIB Enhanced Etch Process," FEI Company 7451 NE Evergreen Parkway; Hillsboro, OR 97124, (1993).

Franklin RE, Kirk ECC, Cleaver JRA, and Ahmed H, Journal of Materials Science Letters 7, 39 (1988).

Gibbons JF, Johnson WS, Mylroie SW, Projected Range Statistics: Semiconductors and Related Materials, Dowden, Hutchinson, and Ross, Inc. Stroudsburg, PA, pp. 3-27. (1975).

Hosler W and Palmer W, Surface and Interface Analysis, 20, 609 (1993).

ICRP 60-1990, "Recommendations of the International Commission on Radiological Protection," in Annals of the ICRP Vol. 21/1-3 Edited by ICRP (1991)

Ishitani T, Tsuboi H, Yaguchi T, and Koike H, "Transmission Electron Microscope Sample Preparation Using a Focused Ion Beam," J. Electron Microsc., Vol 43, pp. 322-26 (1994).

Kempshall BW, Schwarz SM, Prenitzer BI, Giannuzzi LA, and Stevie FA, "Ion Channeling Effects on the FIB Milling of Copper," Journal of Vacuum Science & Technology B, 19(3), 749-754 (May/Jun 2001).

Kola RR, Celler GK, and Harriot LR, Materials Research Society Symposium Proceedings 279, 593 (1993).

Liau, ZL and Mayer, JW, "Ion Bombardment Effects on Material Composition," in Treatise on materials Science and Technology , ed. J K Hirvonen, Academic Press, New York, NY 17-50 (1980)

Lindhard J, Scharff M, and Schiott HE, "Range Concepts on Heavy Ion Ranges" (Notes on Atomic Collisions II), Mat. Fys. Medd. Dan. Vid. Selsk. 33, No. 14, p15. (1963).

Lindhard J, Physics Letters 12, 126 (1964).

Matteson TL, Kempshall BW, Schwarz SW, Houge EC, and Giannuzzi LA, "EBSP Investigation of Focused Ion Beam Surfaces," Journal of Electronic Materials, 31(1), 33-39 (2002).

Nastasi M, Mayer JW and Hirvonen JK, Ion-Solid Interactions: Fundamentals and Applications, Cambridge University Press, Great Britain, (1996).

Onderdelinden D, Applied Physics Letters 8, 189 (1966).

Orloff J, Utlaut M, and Swanson L, High Resolution Focused Ion Beams: FIB and its Applications, Kluwer Academic/Plenum Publishers, NY, (2003).

Palmer W, Wangemann K, Kampermann S, and Hosler W, Nuclear Instruments and Methods in Physics Research B 51, 34 (1990).

Prenitzer BI, Giannuzzi LA, Newman K, Brown SR, Irwin RB, Shofner TL, and Stevie FA, "Transmission Electron Microscope Specimen Preparation of Zn Powders Using the Focused Ion Beam Lift-Out Technique," Met. Trans. A, Vol. 29A, pp. 2399-2405. (1998).

Prenitzer, BI, "Investigation of Variables Affecting Focused Ion Beam Milling as Applied to Specimen Preparation for Electron Microscopy: A Correlation Between Monte Carlo Based Simulation and Empirical Observation, Ph.D. Dissertation, University of Central Florida, (1999).

Rajsiri S, Kempshall BW, Schwarz SM, and Giannuzzi LA, "FIB Damage in Silicon: Amorphization or Redeposition?," Microsc. and Microanal. 8 (Suppl. 2), Microscopy Society of America, 50-51 (2002).

Sigmund, P., Sputtering by Ion Bombardment:Theoretical Concepts, in Sputtering by Particle Bombardment I: Physical Sputtering of Single Element-Solids, R. Behrisch, ed., Topics in Applied Physics vol. 47 (Springer-Verlag, Berlin), (1991).

Sprague JA, Malmberg PR, Reynolds GW, Lambert JM, Treado PA, and Vincenz AM, Nuclear Instruments and Methods in Physics Research B24/25, 572 (1987).

Tartuani M, Takai Y, Shimizu R, Uda K, and TakahashiH, "Development of a Focused Ion Beam Apparatus for Preparing Cross-Sectional Electron Microscope Specimens," Tech. Rep. Osaka Univ., Vol. 43. No. 2143, pp. 167-73. (1993).

Thayer ML, "Enhanced Focused Ion Beam Milling Applications," ISTFA '93, Proc. Int. Symp. Test. Failure Anal., 19th, pp. 425-29 (1993).

Townsend PD, Kelly R, and Hartly NEW, Ion Implantation, Sputtering and Their Applications, Academic Press, pp. 137-42 (1976).

Walker JF, "Focused Ion Beam Applications Using Enhanced Etch," FEI Company 7451 NE Evergreen Parkway; Hillsboro, OR 97124 (1993).

Yamaguchi H, Shimase A, Haraaichi S, and Miyauchi T, "Characteristics of Silicon Removal by Fine Gallium Ion Beam," J. Vac. Sci. Technol. B3(1), pp. 71-4 (1985).

Zeigler JF, Biersack JP, and Littmark U, The Stopping Range of Ions in Solids, Pergamon Press, New York, (1985).

Ziegler, J.F., SRIM 2003, www.srim.org

http://www.springer.com/978-0-387-23116-7

Introduction to Focused Ion Beams
Instrumentation, Theory, Techniques and Practice
Giannuzzi, L.A.; (Eds.)
2005, XVII, 357 p. 34 illus., 28 illus. in color., Hardcover
ISBN: 978-0-387-23116-7